Journal of
Materials Chemistry B

Materials for biology and medicine

ROYAL SOCIETY
OF **CHEMISTRY**
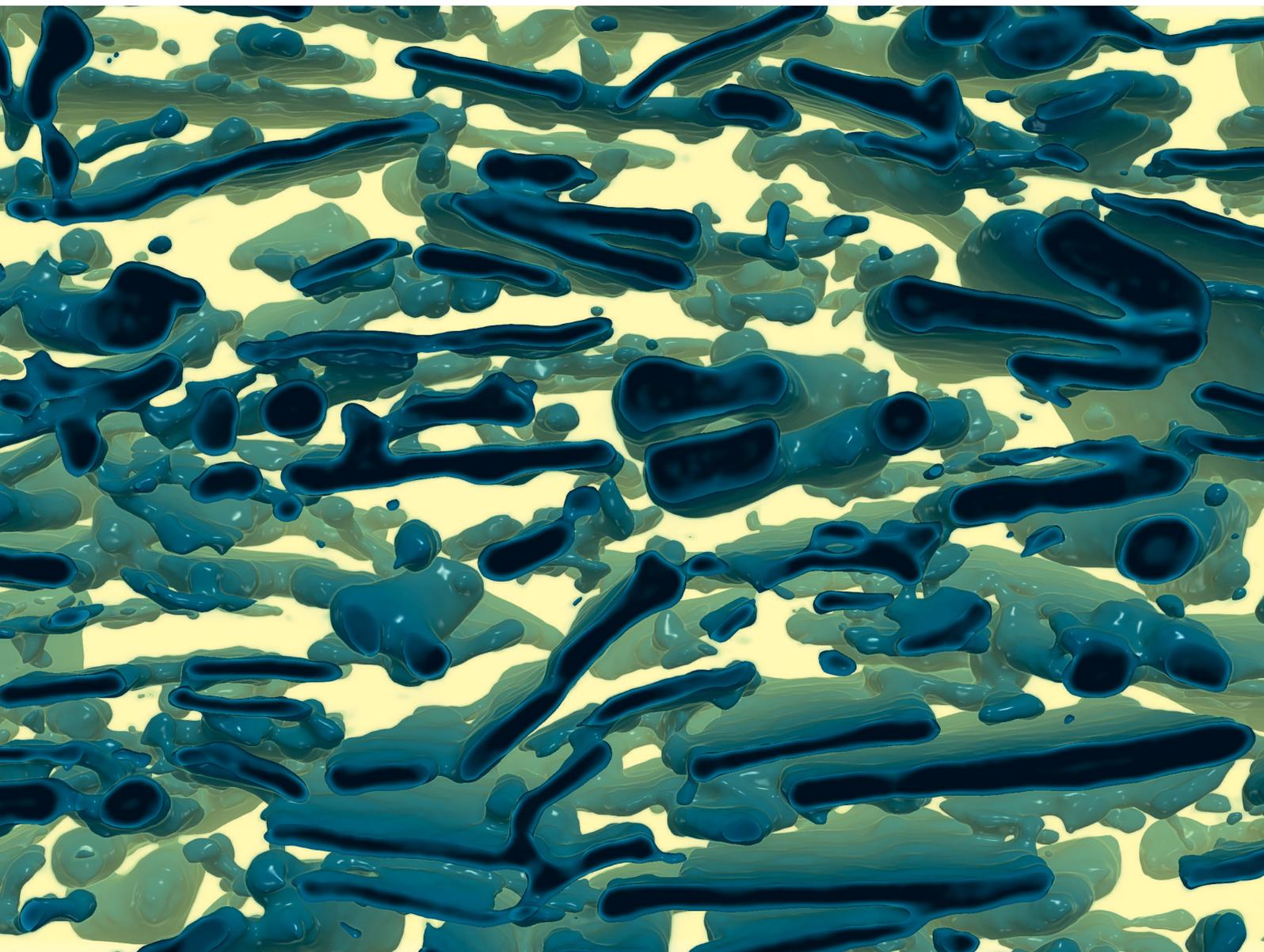
PAPER
José F. Bartolomé *et al.*
A zirconia/tantalum biocermet: *in vitro* and *in vivo* evaluation
for biomedical implant applications

Journal of Materials Chemistry B

Check for updates

A zirconia/tantalum biocermet: *in vitro* and *in vivo* evaluation for biomedical implant applications

Anton Smirnov, [a] Francisco Guitián,[b] Joaquín Ramirez-Rico [cd] and José F. Bartolomé [*e]

A biocermet made of zirconia/20 vol% tantalum (3Y-TZP/Ta) is a new composite with exceptional capabilities due to a combination of properties that are rarely achieved in conventional materials (high strength and toughness, cyclic fatigue resistance and flaw tolerance, wear resistance, corrosion resistance, electrical conductivity, *etc.*). In this study, for the first time, the biomedical performance of a 3Y-TZP/Ta biocermet was evaluated in detail. Its *in vitro* biocompatibility was assessed using mesenchymal stem cell culture. The effectiveness of *in vivo* osteointegration of the biocermet was confirmed 6 months after implantation into the proximal tibiae of New Zealand white rabbits. In addition, the possibility of using magnetic resonance imaging (MRI) for medical analysis of the considered biocermet material was studied. The 3Y-TZP/Ta composite showed no injurious effect on cell morphology, extracellular matrix production or cell proliferation. Moreover, the implanted biocermet appeared to be capable of promoting bone growth without adverse reactions. On the other hand, this biocermet demonstrates artefact-free performance in MRI biomedical image analysis studies, making it more suitable for implant applications. These findings open up possibilities for a wide range of applications of these materials in orthopedics, dentistry and other areas such as replacement of hard tissues.

1. Introduction

Metals and metallic alloys are commonly utilized in total bone replacement or implant fixation due to their mechanical properties that meet the requirements of load-bearing bone applications. Biodegradable alloys have garnered significant attention because of their unique favorable biocompatibility and suitable mechanical properties.[1,2] However, orthopedic traditional non-degradable metallic implants are linked to local and distant negative tissue responses. Typically, these adverse effects are caused by the degradation products of implanted materials, primarily generated through wear and corrosion of metals in bodily fluids.[3] Corrosion releases metal ions that enter the bloodstream and accumulate in red blood cells. Consequently, these metal ions may infiltrate cells and persist in local tissues or disseminate throughout the body, resulting in cytotoxic, genotoxic, and immunological effects, either locally or at a distance from the implant.[4] It has been discovered that in specific cases, the release of nickel (Ni), chromium (Cr), and cobalt (Cr) ions from stainless steel or Co–Cr alloys, respectively, can trigger hypersensitivity reactions and even carcinogenesis.[5–7] Additionally, there is a concern regarding the interplay between magnetic and non-magnetic metallic devices with specific geometries and the magnetic field during magnetic resonance imaging (MRI), which can result in implant heating and even displacement.[8,9] Another consideration is the potential for imaging artifacts that may undermine the effectiveness and quality of the procedure.[10–12]

In the field of biomedicine, ceramics offer significant potential, given their compatibility with the physiological environment, durability, and resistance to wear. Furthermore, ceramics are highly appealing for dental applications due to their chemical stability and aesthetic appeal. However, a number of inherent disadvantages of ceramics limit their widespread application. The brittleness of ceramics, marked by their low fracture toughness, stands out as one of their notable drawbacks. In particular, the influence of the human environment and external loads can lead to rapid growth of microcracks in the contact zone of ceramics with bone or even in the ceramic implant itself and, as a consequence, can lead to final unpredictable failure. In addition, ceramics generally have poor machinability and require the use of expensive diamond tools,

[a] *Federal State Budgetary Educational Institution of the Higher Education Moscow State University of Technology "STANKIN", Moscow, Russian Federation*

[b] *Instituto de Materiales, iMATUS – USC, Santiago de Compostela, Spain*

[c] *Instituto de Ciencia de Materiales de Sevilla, CSIC – Universidad de Sevilla, Avda. Américo Vespucio 49, 41092 Seville, Spain*

[d] *Dpto. Física de La Materia Condensada, Universidad de Sevilla, Avda. Reina Mercedes SN, 41012 Seville, Spain*

[e] *Instituto de Ciencia de Materiales de Madrid (ICMM), Consejo Superior de Investigaciones Científicas (CSIC), Madrid, Spain. E-mail: jbartolo@icmm.csic.es; Tel: +34 91 3348 996*

This journal is © The Royal Society of Chemistry 2024

J. Mater. Chem. B, 2024, **12**, 8919–8928 | **8919**

which also remains an important obstacle to the fabrication of high-performance ceramic implants.[13] The concept of reinforcing brittle ceramics with ductile metals has been employed to enhance the mechanical properties of ceramics.[14–27] The dispersion of metal particles within a ceramic matrix effectively absorbs and disperses the energy of propagating cracks, resulting in an increased fracture toughness of the material. Therefore, given the high attractiveness of using biocompatible metal-reinforced ceramic matrix composites, biocermets have been proposed as a new generation of multifunctional implants for hard tissue replacement with high load-bearing capacity.[28] In recent decades, studies have been mainly conducted on the mechanical and biological properties of bioinert (zirconia and alumina) and bioactive (hydroxyapatite–wollastonite) materials reinforced with niobium, molybdenum, zirconium, titanium, stainless steel and silver particles.[29–40] One of the key benefits of these biocermets is their ability to combine the distinct properties of ceramic and metal components into a single multifunctional material. While biomechanical stability is crucial, biomaterials also need to meet other functional requirements for specific applications. Previous research has highlighted the exceptional capabilities of a zirconia/Ta composite, such as excellent structural properties (fatigue resistance, hardness, etc.),[41–45] high resistance to low-temperature degradation[46] and electrical conductivity that enables electric discharge machining (with a metal content close to the percolation threshold of approximately 16 vol%).[47] Moreover, these biocermets demonstrated the potential to modify their surfaces to enhance fast bone integration[48] and wear resistance[49] and for effective prevention of implant-associated infections (antibacterial properties and bacterial biofilm inhibition).[50,51] Comprehensive characterization of materials intended for biomedical applications includes their chemical, physical, and mechanical properties. Equally important is evaluating their behavior in biological environments and assessing their biocompatibility. While there have been numerous studies on the in vitro and in vivo biocompatibility of ZrO_2 and Ta in their individual forms,[52,53] the biological response of ZrO_2/Ta composites remains an unexplored area of research. On the other hand, it should also be noted that the magnetic susceptibility (χ) of the implant metal plays a major role in MRI diagnostics. The images on different types of devices differ from each other. It is known that the magnetic field strength influences the quality of the images and the speed of visualization. Typically, clinics use tomographs with a magnetic field strength of 1.5 Tesla. This power allows marking the problem area correctly and clear visualization of the tissues. It also gives an opportunity to determine the degree of disturbance with high accuracy. On the other hand, depending on the clinical case (e.g. tumors), a higher power (3 Tesla) is required. Currently, titanium and its alloys are widely used for prosthetics. However, the magnetic susceptibility of titanium is 3.2×10^{-6} cm^3 g^{-1} and that of tantalum is 0.85×10^{-6} cm^3 g^{-1},[54] which makes the latter a prospective material for the use of more powerful tomographs. Moreover, through the introduction of Ta metal into a diamagnetic ceramic matrix with a clear hypointense contrast without generating artifacts or distortions in MRI images,[55] it is possible to further reduce the magnetic

susceptibility, making the resultant biocermet implants more suitable for biomedical image analysis.

Based on our previous work,[41–51] we have selected the optimal composition zirconia/20 vol%Ta with outstanding multifunctional properties, to evaluate its biocompatibility by in vitro and in vivo studies and its compatibility with MRI diagnosis, for possible application as a new biomedical implant material.

2. Materials and methods

2.1. Materials processing

For fabrication of the ceramic–metal mixture the yttria stabilized tetragonal zirconia (3Y-TZP, 3 mol% Y_2O_3; TZ-3YE, Tosoh Corp., Tokyo, Japan) and tantalum (99.97% purity, Alfa Aesar, Karslruhe, Germany) powders with average particle sizes of 0.26 and 44 μm, respectively, have been used as the starting materials. The tantalum powder was first milled in an attritor and then wet mixed with 80 vol% ceramic powder. More detailed information on the starting materials and the powder mixing technique are presented in a previous work.[46] After homogenization, the suspension was dried for 24 h at 75 °C and then passed through a sieve with a mesh size of 32 μm. The resulting mixture was consolidated using spark plasma sintering (SPS) at 1400 °C and 80 MPa in a vacuum. The obtained 3Y-TZP/Ta samples had a diameter and a thickness of 20 and 7 mm, respectively. Details of the sintering regimes were reported elsewhere.[45] Discs (⌀ 20 mm and 2 mm thick) for the in vitro tests and cylinders (∼ 2 mm and height 5 mm) for implantation were made using a diamond tool from sintered disks. Discs cut from a commercially available tantalum (TA007920, ⌀ 20 mm, 99.9% purity, Goodfellow, Huntingdon, England) rod and a 3Y-TZP SPSed monolithic ceramic were used as reference materials for in vitro studies. For in vivo studies, a tantalum rod (TA007950) obtained from the same manufacturer with the same purity, differing only in the diameter (⌀ 2 mm), was chosen as a control material. All the materials were polished with a diamond suspension with the particle size ranging from 9 to 1 μm. Polishing operations were carried out using the polishing machine RotoPol-22 (Struers, Copenhagen, Denmark) at a speed of 150 rpm and a force of 30 N.

2.2. Microstructure characterization

The microstructure of the polished 3Y-TZP/20Ta specimens was studied using a scanning electron microscope VEGA 3 LMH (SEM Tescan, Brno, Czech Republic) equipped with an energy dispersive X-ray spectrometer (EDS), which was employed for the chemical microanalysis of sintered samples.

The 3D microstructure was investigated by high-resolution transmission X-ray tomography using an Xradia Versa 610 XRM system (Zeiss, Jena, Germany) capable of achieving submicrometer resolution. An interior volume of approximately 250 μm × 200 μm × 100 μm was reconstructed using a 20× objective at a voxel size of 270 nm. An acceleration voltage of 140 kV and a current of 150 μA were used, providing sufficient

8920 | J. Mater. Chem. B, 2024, 12, 8919–8928

This journal is © The Royal Society of Chemistry 2024

contrast between the Ta particles and 3Y-TZP matrix. Image segmentation was performed to isolate the Ta phase using a machine learning pixel classificator.[56] The platelet thickness distribution was determined using the BoneJ software.[57]

2.3. *In vitro* study

2.3.1. Isolation and culture of mesenchymal stem/stromal cells (MSCs) derived from bone marrow (BM) cells. Human bone marrow-derived mesenchymal stromal cells (hBMSCs) were employed to evaluate the biocompatibility of the fabricated biocermet. The hBMSCs were provided by the Department of Orthopaedic Surgery (University of Santiago de Compostela Clinical Hospital) from patients undergoing hip replacement surgeries with informed consent. The hBMSCs were isolated from bone marrow samples using heparinized tubes and a Ficoll density gradient method as described by Yeo *et al.*[58] The cells were then washed with Dulbecco's Modified Eagle Medium (DMEM, Sigma-Aldrich, St. Louis, MO, USA) supplemented with 10% fetal bovine serum (FBS, Gibco, Waltham, CA, USA) and seeded onto 75 cm^2 flasks (Sigma-Aldrich, St. Louis, MO, USA). The cells were maintained at 37 °C and 5% CO$_2$ until they reached 90% confluence. Then, the cells were detached and plated onto the tested materials at a density of 60×10^3 cells per cm^2. The cell–material interactions were assessed after 2, 7 and 10 days of culture.

2.3.2. Cell proliferation by MTT assays. The sample discs of pure tantalum, zirconia or biocermet were placed in a 24-well plate. hBMSCs were cultured on the discs at a density of 25×10^3 cells per well. The cell viability and proliferation were assessed by MTT assay at 2, 7 and 10 days of culture. The MTT assay was performed according to the manufacturer's instructions (Sigma-Aldrich, St. Louis, MO, USA). In brief, the cells were incubated with MTT solution overnight, and then the MTT solution was removed. The formazan crystals were dissolved in 100 mL of DMSO by shaking the plate for 15 min, and 50 mL of each well was transferred to a new 24-well plate. The absorbance was measured at 570 nm using an automatic plate reader (PerkinElmer, Boston, MA, USA).

2.3.3. Apoptosis caspase activity assay. The Quantikine ELISA active caspase-3 kit (R&D Systems, Minneapolis, MN, USA) was used to measure caspase-3 activity in supernatants. This kit detects the active caspase-3 by using a biotin-ZVKD-fluoromethyl ketone inhibitor that binds covalently to the protease. The cell lysates were added to a microplate pre-coated with a monoclonal antibody specific for active caspase-3, and the protease levels were determined following the manufacturer's instructions. The cytoplasmic protein extract was incubated with the inhibitor before adding to the microplate.

2.3.4. Cell morphology. To examine the cell morphology, SEM was used. Metallic Ta, zirconia and biocermet substrates were seeded with human bone marrow derived mesenchymal stem cells at a density of 250×10^3 cells per cm^2 and cultured in DMEM supplemented with 20% FBS and gentamicin. The cultures were incubated for 48 hours at 37 °C and 5% CO$_2$. Then, the culture medium was discarded and the cells were rinsed twice with PBS. A fixing solution containing 1% glutaraldehyde and 1% paraformaldehyde was added to the wells and left for 48 h at 25 °C. Finally, the cells were dehydrated by sequential ethanol dilutions.

2.3.5. Confocal microscopy: live/dead staining. Calcein-acetoxymethyl ester (Sigma-Aldrich, St. Louis, MO, USA) and propidium iodide were used to stain hBMSCs cultured on the disks. After 48 h of incubation, samples were gently washed with DMEM and SP2 confocal laser microscopy (Leica, Wetzlar, Germany) was used to visualize viable and nonviable cells; viable cells emitted green fluorescence while nonviable cells emitted red fluorescence.

2.3.6. Statistical analysis. The statistical analysis of the data was performed using Minitab 16, an advanced software developed by Minitab Inc., PA, USA. To assess the significance of the results, Student's t tests were conducted with a significance level of p-value < 0.05 ($n = 10$).

2.4. *In vivo* study

3Y-TZP/Ta and Ta cylinders were implanted in the proximal medial tibia of three adult New Zealand white rabbits (Charlie Rivel, France) weighing approximately 3.5 kg and 9–10 months old. All animal experiments and procedures were performed in accordance with the Scientific Council of the Galician Ceramic Institute, Santiago de Compostela, Spain. The study was conducted according to the protocol 01/2007A, which received institutional approval (January 26, 2009) from the Scientific Council of the Galician Ceramic Institute, Santiago de Compostela, Spain. Animals were premedicated with diazepam 0.2 mL kg^{-1} (Valium 10, Roche, Basel, Switzerland), ketamine 10 mg kg^{-1} (Imalgene 1000, Merial, Lyon, France) and medetomidine 0.1 mg kg^{-1} (Domitor, Orion, Espoo, Finland). Animals were anesthetized by intramuscular injection in the hind legs. The area of the anterior tibialis muscle was shaved. The skin was disinfected with 10% povidone-iodine solution (Betadine, Medapharma, San Fernando de Henares, Spain). Infiltrative articaine (1.5 mL) anesthesia (Ultracain 40/0.005, Normon, Tres Cantos, Spain) was injected subcutaneously into the anterior tibial surface. Cylinders made of sintered and well-polished 3Y-TZP/Ta ceramic–metal composites with a length of 5 mm and a diameter of 2 mm were implanted in each animal with two cylinders in the proximal medial tibia. Surgical preparation of the cylinders was performed using a pilot drill (Precision drill 33071 Nobel Biocare, Barcelona, Spain) followed by a 2 mm twist drill (Twist Drill 32296 Nobel Biocare, Barcelona, Spain). Drilling was carefully performed using a low-speed handpiece (KaVo Intrasurg 300, Madrid, Spain), not exceeding 2000 rpm and cooled with a large volume of saline solution. A metal rod was used for the right tibia and a 3Y-TZP/Ta biocermet for the left tibia. All cylinders were separated by at least 10 mm. The cylinders were impacted using the hammer blow method and the surface edges were flossed with bone. The periosteum was sutured with continuous monofilament absorbable sutures (3-0 Monocryl, Ethicon, Madrid, Spain). The skin was sutured with intermittent threaded absorbable sutures (Vicryl 3-0, Ethicon, Madrid, Spain). The skin was again immersed in povidone-iodine solution; six months later, the rabbits were euthanized by lethal injection of ketamine/diazepam.

This journal is © The Royal Society of Chemistry 2024

J. Mater. Chem. B, 2024, **12**, 8919–8928 | **8921**

2.4.1. Histological preparation and examination. After euthanasia, the entire tibia was removed and the exact location of the implant was determined by radiographic examination. The tibia was fixed in buffered formalin (10%) for one week. The two implants in each tibia were separated and each specimen was reduced in size; the specimens were dehydrated by immersion in a concentrated alcohol solution according to the Donath and Breuner method.[59] The samples were infiltrated with Technovit 7200 resin (Kulzer, Madrid, Spain). After photopolymerization of the infiltrated blocks, thin polished slides were obtained. Samples were stained with Papanicolaou-Harris hematoxylin (Merck, Darmstadt, Germany) and Wheatley's Slichro stain (Chromotrope 2R, Newcomer supply, Middleton, WI, USA) followed by Canada Balsam solution (Fluka Biochemika, Alcobendas, Madrid, Spain); samples were observed using a transmission light microscope (Optiphot, Nikon, Tokyo, Japan) equipped with a DP-12 digital camera (Olympus, Tokyo, Japan).

2.4.2. Histomorphometric evaluation. Histomorphometry was performed using an SZX12 microscope (Olympus, Tokyo, Japan) equipped with an Olympus DP12 camera. The acquired images were processed using image J-1.46r software (Bethesda, MD, USA) to determine the bone-to-implant contact (BIC) ratio, defined as the proportion of bone in direct contact with the implant surface. If necessary, polarized light microscopy was used to determine the boundaries of the newly formed bone. All measurements were performed by the same investigator and boundaries were corrected by another investigator. To quantify repeatability and measurement error, five randomly selected slides were measured three times over a three-day period.[60] BIC evaluation was performed using eight measurements per cylinder.

2.4.3. Statistical analysis. To test the normality of the histomorphometry data, a K–S test was conducted. Subsequently, the means were compared using the Wilcoxon signed-rank test. The statistical analysis was performed using the IBM-SPSS 18.0 software package (Chicago, IL, USA). The significance level was defined as $P < 0.05$.

2.5. Magnetic resonance imaging (MRI) compatibility

SPSed 3Y-TZP/Ta samples were semi-vertically immersed in an agarose gel containing saline (1.6%). Magnetic resonance imaging studies were performed on a 9.4 T MRI system (Bruker Biospin, Ettlingen, Germany) with a 440 mT m^{-1} gradient, a 7 cm diameter linear birdcage resonator for signal transmission and a 2×2 array surface coil for signal detection (both used in combination with Bruker Biospin, Ettlingen, Germany). Spin-echo (T1 and T2), gradient recall echo (GRE) and echo planar imaging (EPI) were selected as typical clinical MRI sequence parameters, similar to routine clinical protocols. All MRI experiments were performed at the Institute of Clinical Neuroscience of the Clinical Hospital of the University of Santiago de Compostela (Santiago de Compostela, Spain).

3. Results and discussion

The electron micrograph of the microstructure of the sintered 3Y-TZP/Ta composite is shown in Fig. 1. In this micrograph, the dark phase represents 3Y-TZP and the gray phase represents Ta grains, as confirmed by the complementary EDS compositional analysis. The tantalum grains are homogeneously distributed in the zirconia matrix and no pores are observed.

Fig. 2A shows the constructed 3D image of the 3Y-TZP/Ta structure. The continuous zirconia matrix and the tantalum particles (shown in yellow-green) entangle each other and form a three-dimensional network structure. Fig. 2B shows the thickness of the Ta phase. The Ta phase shows a well-defined distribution with a median plate thickness of ~ 2 μm.

Previous studies[47,50] have shown that this particular distribution of the lamellar metallic phase in the microstructure of the composite material means that its resistance to crack growth is much higher than that of monolithic zirconia. The major contributions to toughening are the resulting crack bridging and plastic deformation of the metallic particles, together with crack deflection and interfacial debonding. The intricate interplay of multiphase and multiscale mechanisms within these materials hinders crack propagation, leading to a remarkable toughness of 16 MPa m$^{1/2}$ (Table 1). Not only does this value exceed that of conventional commercial bioceramics, but this ceramic–metal composite also demonstrates a very high resistance to cyclic fatigue, which is critical for long-term durability.[49] As a result, these composites exhibit an unprecedented combination of high toughness, strength, damage tolerance and fatigue resistance due to their unique microstructure.

To assess the biocompatibility of these materials, mesenchymal cells are chosen for this experiment because they are considered as important cells to test new materials, as primary cells are known to have an unaltered cytoskeleton and growth pattern compared to cell lines such as Saos-2.[61] The proliferation of mesenchymal stem cells on substrates is shown in Fig. 3. The cells were plated on each substrate and incubated on various substrates for 2, 7 and 10 days; MTT assay results are shown as mean ± standard deviation. 3Y-TZP/Ta composites have a similar biocompatibility to pure Ta (p-value > 0.05, Student's t test, 95% confidence level) for each time point. Thus, no significant differences were assumed between these two groups. On the other hand, the 3Y-TZP/Ta composite shows a larger proliferation rate
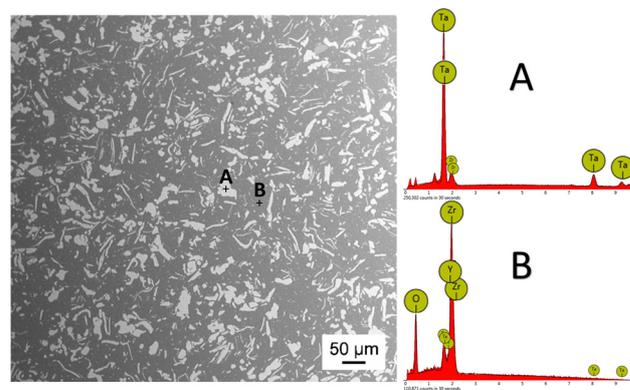

Fig. 1 SEM image of a polished surface of a 3Y-TZP/Ta sintered composite and EDS spectra taken at two points on the surface marked with crosses corresponding to (A) the tantalum grain and (B) the zirconia matrix.
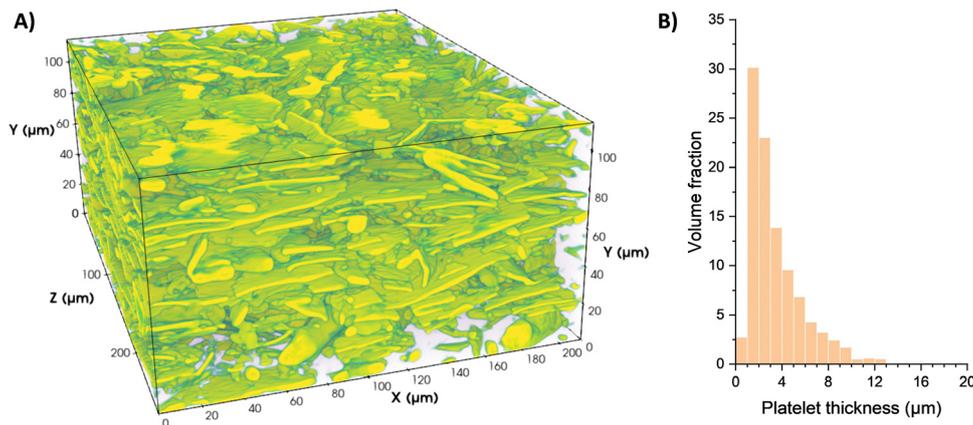
8922 | *J. Mater. Chem. B*, 2024, **12**, 8919–8928

This journal is © The Royal Society of Chemistry 2024

Fig. 2 (A) Segmented 3D image of the Ta particles showing its plate-like morphology and high degree of entanglement. (B) Histogram of platelet thickness, showing a well-defined distribution and a median thickness of ~2 μm.

Table 1 A summary of the mechanical properties of the 3Y-TZP/Ta composite in comparison with the 3Y-TZP ceramic obtained under similar conditions[47,49,50]

	Density [% φ_{th}]	Elastic modulus E [GPa]	Flexural strength σ_f [MPa]	Hardness HV [GPa]	Fracture toughness K_{Ic} [MPa m$^{1/2}$]
3Y-TZP	99	198 ± 5	1217 ± 10	13 ± 0.3	6 ± 0.3
3Y-TZP/Ta	98	194 ± 7	970 ± 18	9 ± 0.7	16 ± 0.9

than 3Y-TZP (p-value < 0.05, Student's t test, 95% confidence level) after 10 days of incubation, showing that the composite material is more prone to cell colonization.

Fig. 4 shows a steady increase in caspase 3 activity in all samples in relation to the rate of intrinsic apoptosis in culture. However, no significant differences were found between 3Y-TZP, Ta and 3Y-TZP/Ta for each time point studied (p-value > 0.05, Student's t test, 95% confidence level). A nominal apoptotic rate is always found in cell cultures even on cell friendly surfaces of culture flasks.

From the *in vitro* results obtained, it can be concluded that pure Ta and 3Y-TZP/Ta composites promote a higher cell proliferation than 3Y-TZP monolithic ceramics, which facilitates cell colony formation. SEM imaging of hBMSCs cultured for 48 hours on the fabricated substrates (Fig. 5) revealed that in all samples adhesion, cell spreading and proliferation were clearly observed. However, in the case of the biocermet material almost the entire surface is covered with cells and a large amount of extracellular matrix is visible (Fig. 5D).

Confocal microscopy showed that cell proliferation and viability were optimal on both Ta and 3Y-TZP/Ta surfaces (Fig. 6). After 10 days of incubation, the 3Y-TZP/Ta biocermet
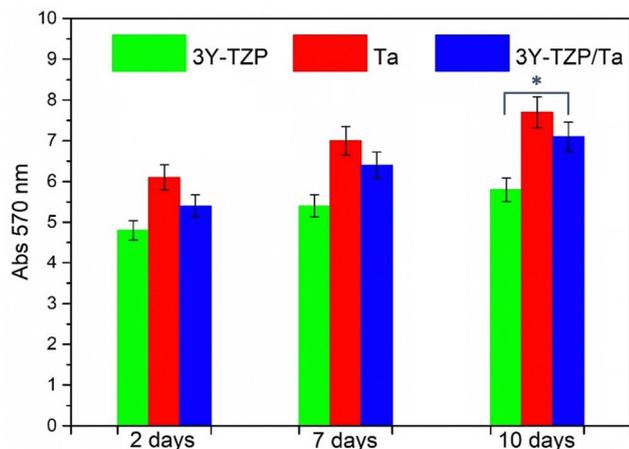

Fig. 3 Cell proliferation results according to absorbance values of the samples after incubation for different times. The significant difference is connected by a horizontal line (*p < 0.05). p-Values for 2 and 7 days are above 0.05, thus assuming no significant differences.
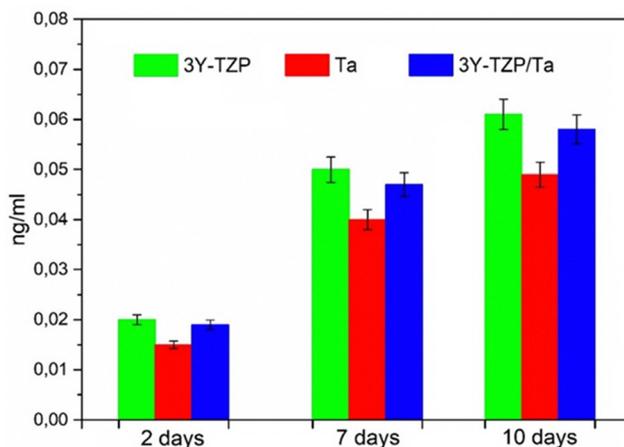

Fig. 4 Caspase assay results for all studied materials. No significant differences were found between groups (p > 0.05).
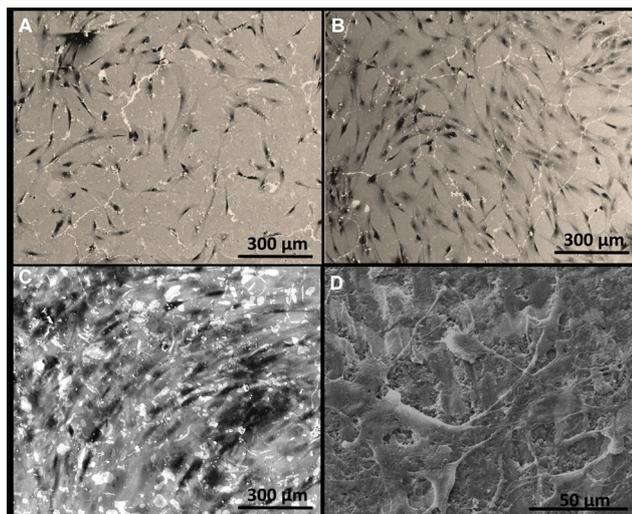
This journal is © The Royal Society of Chemistry 2024

J. Mater. Chem. B, 2024, **12**, 8919–8928 | **8923**

Fig. 5 Scanning electron micrographs of mesenchymal stem cells plated onto the 3Y-TZP (A), Ta (B) and 3Y-TZP/Ta (C) and (D) substrates.
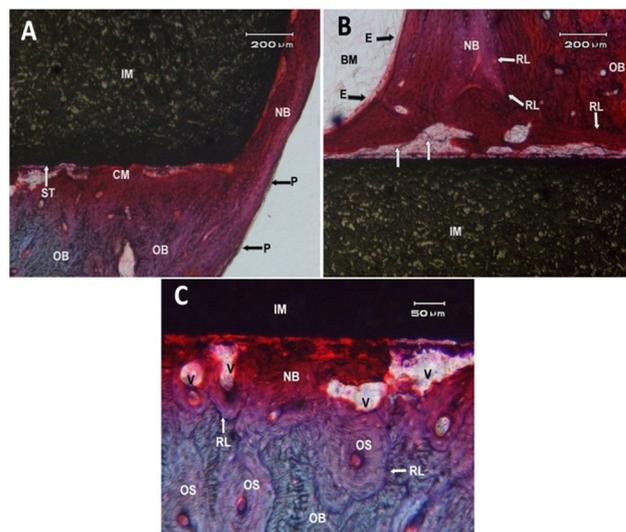

Fig. 7 Bone-biocermet implant interface: General view (A and B) and detailed close-up (C). The surface end of the implant rod made of the 3Y-TZP/Ta biocermet (IM), new bone (NB), old bone (OB), periosteum (P), mineralized zone (CM), unmineralized zone (ST) within the matrix, tibia's medullary cavity (BM), endosteum (E), cement reversal lines (RL), vascular structures (V), Haversian systems (osteons) (OS) and cemental lines (RL).

shows a high concentration of cells on the surface. On the other hand, zirconia samples were not so colonized, confirming the observations from MTT assays.

However, the complex biological processes that occur between the implant and the bone/tissue cannot be completely simulated under laboratory conditions. Therefore, further *in vivo* studies were conducted to confirm the findings of *in vitro* experiments. Histological observations 6 months after implant placement in the proximal medial tibia of New Zealand white rabbits showed that there was some immature new bone in the new bone area of both 3Y-TZP/Ta biocermet and pure metal materials (Fig. 7 and 8). Fig. 7A shows the surface end of the implant rod made of the 3Y-TZP/Ta biocermet (IM), displaying the formation of new bone (NB) originating from the neighboring diaphyseal old bone (OB) and the periosteum (P). At the interface between the implant and tissue, distinct contact zones were identified: a mineralized zone (CM) and an unmineralized zone (ST) within the matrix. Fig. 7B shows the surface of the 3Y-TZP/Ta biocermet rod at the entrance of the tibia's medullary cavity (BM) stimulating the formation of new bone (NB) along the surface of the stabilized implant (IM) through the influence of the endosteum (E). Cement reversal lines (RL) were observed between the compact Haversian old

bone (OB) and the newly formed bone with a lamellar structure characterized by plexiform features. It's important to note the extensive vascularization of the new bone originating from the nearby diaphyseal old bone (OB). Some points at the interface displayed a lack of mineralization, which can be observed through the vertical white arrows. Fig. 7C gives a closer look at the interface between the bone and the implant, revealing the process of bone remodeling (NB) occurring in direct contact with vascular structures (V), separated from the Haversian systems (osteons) (OS) of the old bone (OB) by cemental lines (RL).

Fig. 8A shows the end surface of a rod made of tantalum (IM), revealing the formation of new bone (NB) originating from the periosteal surface (P) on the front-inner side of the tibia's diaphysis. The observation included the presence of old compact bone consisting of Haversian structures (OS), vascular spaces (V), and cemental lines (RL). Fig. 8B shows that the interphase zone of the implant (IM) within the medullary cavity (CM) was characterized by the presence of a cemental line (RL)
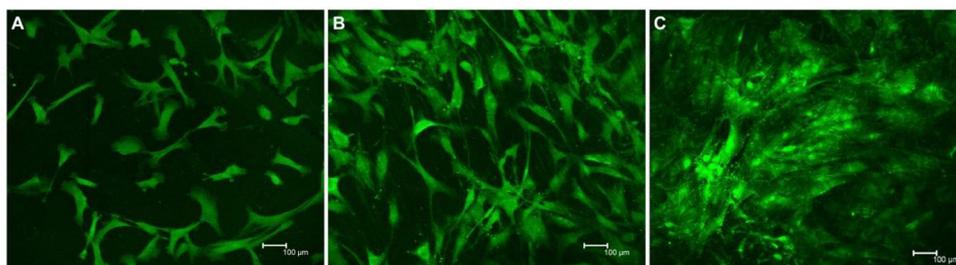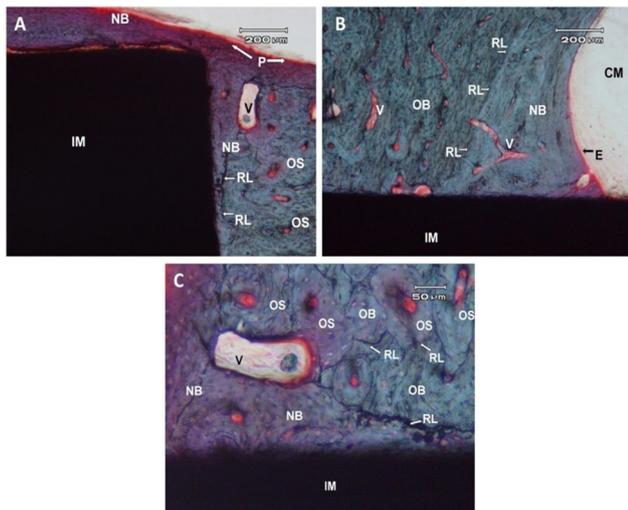

Fig. 6 Confocal laser scanning microscope image of the hBMSCs grown on: 3Y-TZP (A), Ta (B) and 3Y-TZP/Ta (C) surfaces during culture for 10 days. hBMSCs were stained with green fluorescent calcein AM.

8924 | J. Mater. Chem. B, 2024, 12, 8919–8928

This journal is © The Royal Society of Chemistry 2024

Fig. 8 Bone-tantalum implant interface: General view (A and B) and detailed close-up (C). The end surface of a rod made of tantalum (IM), new bone (NB), periosteal surface (P), Haversian structures (OS), vascular spaces (V), cemental lines (RL), interphase zone of the implant (IM), medullary cavity (CM), cemental lines (RL), and endosteal (E) and compact old bone (OB).

separating the endosteal (E) new bone (NB) from the surrounding compact old bone (OB). It is worth noting the passage of new vascularization through the cemental lines (V). Fig. 8C shows a close view of the bone–implant interface, revealing the close apposition of a newly formed, highly vascularized bone (NB) to the surface of the implant. Cemental lines (RL) acted as boundaries between the old bone (OB) and the new bone (NB), as well as between the Haversian systems (OS) of the old bone (OB).

These new bone tissues were in direct contact with the Ta metal and 3Y-TZP/Ta biocermet, and no fibrous tissue was observed at the interface between the implant and the new bone. Histological examination of these implants did not show any inflammatory reaction. Complete stabilization of the 3Y-TZP/Ta biocermet cylinder was observed at the tibial diaphysis (Fig. 7). The superficial and apical ends of the implants were completely covered with the new bone. Moreover, the implanted cylinder also shows osteoconductivity as some of the new bone grows from the endosteum of the implant surface. However, this new bone shows an irregular lamellar structure. At the bone–implant interface, the new bone is immature and poorly structured. The osteocyte spaces are filled by typical osteocytes, but show a heterogeneous distribution around neoplastic vascular structures close to the implant. This difference reduces the contact area between the implant and the calcified matrix interface, resulting in immaturity of the new bone. No inflammatory reaction was observed at any site and the implant surfaces were well adapted to the bone marrow in the medullary cavity. Continuous bonding of the mineralized bone matrix in direct contact with the tantalum rod surface was clearly observed (Fig. 8). The stabilization of the tantalum implant in the tibial diaphysis is due to the close contact between the compact bone and the metal rod surface.

The newly formed bone covers the scar tissue around the implant contact area and the old bone shows highly vascularized plexiform structures arising from the periosteum and endosteum. The newly formed bone covers the superficial and apical ends of the rod. A new layer of bone formed from the endosteum stabilizes the implant along the medullary cavity. This bone is highly vascularized and has a braided and lamellar structure. In the implant contact area, the new bone is less mineralized and cement lines define the boundaries of the new bone. Osteocytes are evenly distributed at the bone/implant interface. No evidence of dysplasia or inflammatory or connective tissue interposition at the interface is observed. Bone marrow is strongly angiogenic and in close contact with the implant, with no evidence of an inflammatory response. The bone volume and bone–implant contact area were larger in tantalum metal rods than in the composite. The bone-to-implant contact (BIC) values were $55.3 \pm 6.3\%$ for the 3Y-TZP/Ta biocermet and $80.4 \pm 5.2\%$ for the tantalum rods, with a significant difference between the groups for $p < 0.04$. The high BIC value of tantalum cylinders confirms the results obtained *in vitro* and thus confirms the excellent biocompatibility of tantalum metal. On the other hand, the value obtained for the 3Y-TZP/Ta biocermet is in good agreement with that reported for the zirconia–niobium system.[38] Therefore, the 3Y-TZP/Ta composite was found to be a biocompatible material capable of facilitating osteointegration.

The behavior of the developed biocermet during the MRI study was also evaluated. The different types of images shown in Fig. 9 are related to signal heterogeneity and noise and to the repetition time (TR) and echo time (TE) of the MRI protocol. The gradient recall echo sequence (GRE) method is more versatile than other techniques and allows the spin flip and tip angles to be varied in addition to the usual TR and TE parameters, resulting in clearer images. Echo-planar imaging (EPI) is the fastest imaging method in MRI, but has limited spatial resolution and causes high distortion. Spin-echo (SE) pulse sequences are the most commonly used pulse sequences. $T1$- and $T2$-weighted images can be obtained by adjusting the timing of the pulse sequence: short TR and short TE result in a $T1$-weighted image, while long TR and long TE result in a $T2$-weighted image. None of the ceramic–metal composite materials' GRE examined produced a detectable strain (Fig. 9A). The spin-echo pulse sequence showed negligible distortion (Fig. 9B and C), while distortion was slightly higher on echo-planar images, as expected (Fig. 9D). In conclusion, no significant image artefacts were observed during the MRI examination, confirming the compatibility of this medical imaging technique with the studied 3Y-TZP/Ta biocermet.

Previous studies have observed that zirconia implants are favorable in terms of low artifacts compared with metal implants.[62–64] When tantalum, a paramagnetic material, was combined with diamagnetic materials, such as zirconia (susceptibility: -8.3×10^{-6} [54]), almost no artifacts were noted in the MRI according to our investigation. Previous research also observed reduced artifact size when a paramagnetic NiTi implant was coated with diamagnetic graphene oxide and carbon nanotubes,
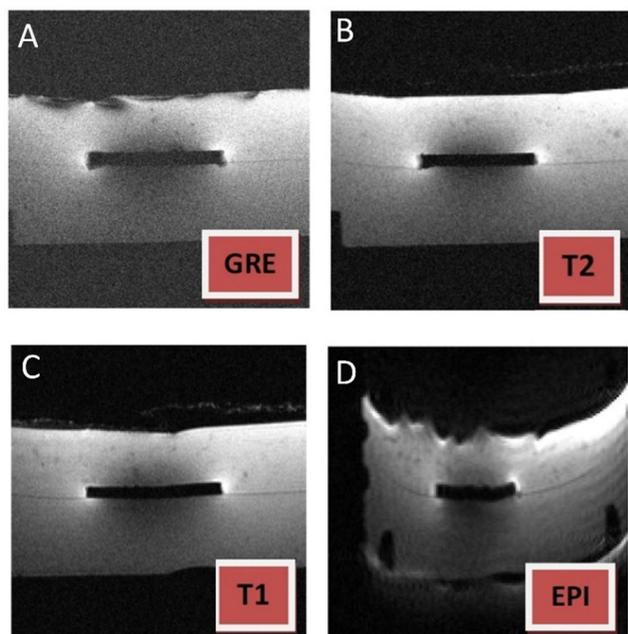
This journal is © The Royal Society of Chemistry 2024

J. Mater. Chem. B, 2024, **12**, 8919–8928 | **8925**

Fig. 9 MR tomographic images of the 3Y-TZP/Ta biocermet in gradient echo (A), spin echo (B) and (C) and echo-planar imaging (D) modes.

which was in consistence with our results.[65] Moreover, a theoretical study[66] has proposed that combining two materials with different magnetic susceptibilities results in the desired effective magnetic susceptibility. Calculations indicate that susceptibility artifacts can be well suppressed by combining paramagnetic and diamagnetic materials. Therefore, we demonstrated the feasibility of MR as a valuable imaging tool for investigating the 3Y-TZP/Ta biocermet in diagnosing post-operative complications following implant surgery and imaging anatomy adjacent to implants. Further validation in patients is required, as this *in vitro* investigation is not able to simulate the impact of the implant's surrounding tissues on MR imaging results *in vivo*.

4. Conclusions

In this paper, *in vitro* and *in vivo* evaluation of a zirconia/20 vol% tantalum (3Y-TZP/Ta) biocermet for biomedical implant applications is performed. Compared to monolithic zirconia, the 3Y-TZP/Ta composite exhibits a significantly higher cell viability. Moreover, this biocermet does not negatively affect cell proliferation, extracellular matrix production, or cell morphology. As a result, the studied 3Y-TZP/Ta biocermet creates a surface that is more favorable for cell growth. These findings from *in vitro* investigations align closely with the results of *in vivo* studies. *In vivo* studies have confirmed the effectiveness of osseointegration within the specified timeframe. The surface of the 3Y-TZP/Ta implant demonstrates high biocompatibility, with no evidence of gaps, fibrous tissue, multinucleated cells, or inflammatory cell infiltration at the bone–implant interface. Additionally, the MRI image quality of the 3Y-TZP/Ta biocermet is not affected by artifacts, unlike other biometal materials. This makes it more suitable for implant applications, as it can

provide accurate and reliable diagnosis of the implant site and surrounding tissues. Overall, these results signify the suitability of the 3Y-TZP/Ta biocermet for orthopedic and dental applications, indicating its significant clinical potential.

Author contributions

Anton Smirnov: writing – original draft, visualization, investigation, data curation; Francisco Guitián: writing – reviewing and editing, visualization, investigation, data curation, conceptualization; Joaquín Ramirez-Rico: writing – reviewing and editing, data curation; and José F. Bartolomé: writing – reviewing and editing, visualization, investigation, data curation, conceptualization.

Data availability

The data that support the findings of this study are available from the corresponding author upon reasonable request.

Conflicts of interest

The authors declare that they have no known competing financial interests or personal relationships that could have appeared to influence the work reported in this paper.

Acknowledgements

References

1 Ch Ling, Q. Li, Z. Zhang, Y. Yang, W. Zhou, W. Chen, Z. Dong, Ch Pan and C. Shuai, *Int. J. Extrem. Manuf.*, 2024, **6**, 015001.

2 M. Yang, C. Chen, D. Wang, Y. Shao, W. Zhou, C. Shuai, Y. Yang and X. Ninget, *J. Magnesium Alloys*, 2024, **12**, 1260–1282.

3 J. Enderle and J. Bronzino, *Introduction to Biomedical Engineering*, 3rd edn, Academic Press, Kidlington, 2012.

4 P. F. Doorn, P. A. Campbell, J. Worrall, P. D. Benya, H. A. McKellop and H. C. Amstutz, *J. Biomed. Mater. Res.*, 1998, **42**, 103–111.

5 H. Pandit, G. S. Jones, S. P. McLardy, R. Gundle, D. Whitwell, C. L. Gibbons, S. Ostlere, N. Athanasou, H. S. Gill and D. W. Murray, *J. Bone. Joint. Surg. Br.*, 2008, **90**, 847–851.

6 N. J. Hallab and J. J. Jacobs, *Bull. NYU. Hosp. Jt. Dis.*, 2009, **67**, 182–188.

7 M. Bahraminasab, B. B. Sahari, K. L. Edwards, F. Farahmand, M. Arumugam and T. S. Hong, *Mater. Des.*, 2012, **42**, 459–470.

8 S. Wildermuth, C. L. Dumoulin, T. Pfammatter, S. E. Maier, E. Hofmann and J. F. Debatin, *Cardiovasc. Intervent. Radiol.*, 1998, **21**, 404–410.

9   P. F. New, B. R. Rosen, T. J. Brady, F. S. Buonanno, J. P. Kistler, C. T. Burt, W. S. Hinshaw, J. H. Newhouse, G. M. Pohost and J. M. Taveras, *NMRI Radiol.*, 1983, **147**, 139–148.

10 F. Shafiei, E. Honda, H. Takahashi and T. Sasaki, *J. Dent. Res.*, 2003, **82**, 602–606.

11 H. Matsuura, T. Inoue, H. Konno, M. Sasaki, K. Ogasawara and A. Ogawa, *J. Neurosurg*, 2002, **97**, 1472–1475.

12 H. Matsuura, T. Inoue, K. Ogasawara, M. Sasaki, H. Konno, Y. Kuzu, H. Nishimoto and A. Ogawa, *Neurol. Med. Chir.*, 2005, **45**, 395–399.

13 V. Bharathi, A. R. Anilchandra, S. S. Sangam, S. Shreyas and S. B. Shankar, *Mater. Today Proc.*, 2021, **46**, 1451–1458.

14 T. Rodriguez-Suarez, J. F. Bartolomé and J. S. Moya, *J. Eur. Ceram. Soc.*, 2011, **32**, 3887–3898.

15 A. Mattern, B. Huchler, D. Staudenecker, R. Oberacker, A. Nagel and M. Hoffmann, *J. Eur. Ceram. Soc.*, 2004, **24**, 3399–3408.

16 I. Ibrahim, F. Mohamed and E. Lavernia, *J. Mater. Sci.*, 1991, **26**, 1137–1156.

17 J. A. Yeomans, *J. Eur. Ceram. Soc.*, 2008, **28**, 1543–1550.

18 K. Kameo, K. Friedrich, J. F. Bartolome, M. Diaz, S. Lopez-Esteban and J. S. Moya, *J. Eur. Ceram. Soc.*, 2003, **23**, 2867–2877.

19 M. Díaz, J. F. Bartolomé, J. Requena and J. S. Moya, *J. Eur. Ceram. Soc.*, 2000, **20**, 1907–1914.

20 J. S. Moya, M. Díaz, C. F. Gutierrez-Gonzalez, L. A. Diaz, R. Torrecillas and J. F. Bartolomé, *J. Eur. Ceram. Soc.*, 2008, **28**, 479–491.

21 R. Torrecillas, A. M. Espino, J. F. Bartolomé and J. S. Moya, *J. Am. Ceram. Soc.*, 2000, **83**, 454–456.

22 J. F. Bartolome, M. Diaz and A. P. Tomsia, *JECS*, 2004, **24**, 785–790.

23 C. Pecharroman, S. Lopez-Esteban and J. S. Moya, *JECS*, 2001, **84**, 2439–2441.

24 T. Rodriguez-Suarez, S. Lopez-Esteban, J. F. Bartolome and J. S. Moya, *J. Eur. Ceram. Soc.*, 2007, **27**, 3339–3344.

25 S. Lopez-Esteban, J. F. Bartolome and T. Tanimoto, *J. Mater. Res.*, 2002, **17**, 1592–1600.

26 C. Pecharroman, F. Esteban-Betegon and J. S. Moya, *Nano Lett.*, 2004, **4**, 747–751.

27 J. S. Moya, S. Lopez-Esteban and J. F. Bartolome, *J. Am. Chem. Soc.*, 2002, **85**, 2119–2121.

28 C. Gao, M. Yao, C. Shuai, P. Feng and S. Peng, *BioDes. Manuf.*, 2020, **3**, 307–330.

29 A. Arifin, A. B. Sulong, N. Muhamad, J. Syarif and M. I. Ramli, *Mater. Des.*, 2014, **55**, 165–175.

30 M. Diaz, A. Smirnov and J. F. Bartolome, *Ceramics*, 2002, **3**, 53–64.

31 D. K. Pattanayak, R. C. Prasad, B. T. Rao and T. R. R. Mohan, *J. Am. Ceram. Soc.*, 2006, **89**, 2172–2176.

32 J. F. Bartolomé, C. F. Gutiérrez-González and R. Torrecillas, *Compos. Sci. Technol.*, 2008, **68**, 1392–1398.

33 C. F. Gutierrez-Gonzalez and J. F. Bartolomé, *J. Mater. Res.*, 2008, **23**, 570–578.

34 S. Lopez-Esteban, J. F. Bartolome and J. S. Moya, *JECS*, 2002, **22**, 2799–2804.

35 S. Nath, S. Kalmodia and B. Basu, *J. Mater. Sci.: Mater. Med.*, 2010, **21**, 1273–1287.

36 Q. Chang, D. L. Chen, H. Q. Ru, X. Y. Yue, L. Yu and C. P. Zhang, *Biomate*, 2010, **31**, 1493–1501.

37 E. Fernandez-Garcia, J. Guillem-Marti, C. F. Gutierrez-Gonzalez, A. Fernandez, M. P. Ginebra and S. Lopez-Esteban, *J. Biomater. Appl.*, 2015, **29**, 813–823.

38 J. F. Bartolomé, J. S. Moya, R. Couceiro, C. F. Gutiérrez-González, F. Guitián and A. Martinez-Insua, *Biomaterials*, 2016, **76**, 313–320.

39 P. Wei, J. Fang, L. Fang, K. Wang, X. Lu and F. Ren, *Appl. Mater. Today.*, 2019, **15**, 531–542.

40 M. Rahaman, T. Huang, B. Bal and Y. Li, *Acta Biomater.*, 2010, **6**, 708–714.

41 A. Jorge-Mora, N. Imaz, N. Frutos, A. Alonso, C. Garcia Santiago, R. Gomez-Vaamonde, J. Pino-Minguez, J. F. Bartolome, G. O'Connor and D. Nieto, *Laser Ablation - From Fundamentals to Applications*, Rijeka, Croatia, 2018.

42 C. Kunz, J. Bonse, D. Spaltmann, C. Neumann, A. Turchanin, J. F. Bartolome, F. A. Muller and S. Graff, *Appl. Surf. Sci.*, 2020, **499**.

43 L. Esteban-Tejeda, A. Smirnov, C. Prado, J. S. Moya, R. Torrecillas and J. F. Bartolomé, *Ceram. Int.*, 2016, **42**, 7023–7029.

44 A. Smirnov and J. F. Bartolomé, *Ceram. Int.*, 2014, **40**, 1829–1834.

45 A. Smirnov, M. Volosova, P. Peretjagin and J. F. Bartolome, *Ceram. Int.*, 2018, **44**, 1404–1410.

46 A. Smirnov, J. F. Bartolomé, H. D. Kurland, J. Grabow and F. A. Müller, *J. Am. Ceram. Soc.*, 2016, **99**, 3205–3209.

47 A. Smirnov, P. Peretyagin and J. F. Bartolomé, *J. Alloys Compd.*, 2018, **739**, 62–68.

48 A. Smirnov, P. Peretyagin and J. F. Bartolomé, *J. Eur. Ceram. Soc.*, 2019, **39**, 3491–3497.

49 A. Smirnov, J. I. Beltrán, T. Rodriguez-Suarez, C. Pecharromán, M. C. Muñoz, J. S. Moya and J. F. Bartolomé, *Sci. Rep.*, 2017, **7**, 449.

50 A. Smirnov and J. F. Bartolomé, *J. Eur. Ceram. Soc.*, 2012, **32**, 3899–3904.

51 A. Smirnov, O. Yanushevich, N. Krikheli, N. W. Solis Pinargote, P. Peretyagin, S. Grigoriev, L. Alou, D. Sevillano, R. López-Piriz, F. Guitian and J. F. Bartolome, *Antibiotics*, 2024, **13**, 175.

52 H. Aifang, J. K. H. Tsoi, C. Y. K. Lung and J. P. Matinlinna, *Dent. Mater. J.*, 2020, **39**, 523–530.

53 G. Mani, D. Porter, K. Grove, S. Collins, A. Ornberg and R. Shulfer, *J. Biomed. Mater.*, 2022, **110**, 1291–1306.

54 A. Mehjabeen, T. Song, W. Xu, H. P. Tang and M. Qian, *Adv. Eng. Mater.*, 2018, **20**, 1800207.

55 Y. Modinger, E. D. Anttila, G. M. Baker, D. C. Gross and A. A. Porporati, *Arthroplasty Today*, 2023, **22**, 101170.

56 S. Berg, D. Kutra, T. Kroeger, C. N. Straehle, B. X. Kausler, C. Haubold, M. Schiegg, J. Ales, T. Beier, M. Rudy, K. Eren, J. I. Cervantes, B. Xu, F. Beuttenmueller, A. Wolny, C. Zhang, U. Koethe, F. A. Hamprecht and A. Kreshuk, *Nat. Methods*, 2019, **16**(12), 1226–1232.

57 M. Doube, M. M. Kłosowski, I. Arganda-Carreras, F. P. Cordelières, R. P. Dougherty, J. S. Jackson, B. Schmid, J. R. Hutchinson and S. J. Shefelbine, *Bone*, 2010, **47**(6), 1076–1079.

This journal is © The Royal Society of Chemistry 2024

J. Mater. Chem. B, 2024, **12**, 8919–8928 | **8927**

58 C. Yeo, *et al.*, *Regen. Med.*, 2009, **4**, 689–696.

59 K. Donath and G. A. Breuner, *J. Oral Pathol.*, 1982, **11**, 318–326.

60 S. M. Yezerinac, S. C. Lougheed and P. Handford, *Syst. Biol.*, 1992, **41**, 471–482.

61 L. Cy, S. Gao, T. Terashita, T. Shimokawa, H. Kawahara, S. Matsuda and N. Kobayashi, *Cell Tissue Res.*, 2006, **324**, 369–375.

62 F. Duttenhoefer, M. E. Mertens, J. Vizkelety, F. Gremse, V. A. Stadelmann and S. Sauerbier, *Clin. Oral Implant Res.*, 2015, **26**, 1195.

63 X. Gao, Q. Wan and Q. Gao, *Sci. Rep.*, 2022, **12**, 428.

64 T. Kamishima, N. Kitamura, M. Amemiya, K. Ishizaka, F. Kato, K. Yasuda, H. Shirato and S. Terae, *Clin. Radiol.*, 2010, **65**, 387e90.

65 T. Hana, Y. Sohna, S. J. Parka, Y.-C. Kim, K. S. Lee, H. S. Kim, S.-G. Yoon, D. Kim and J. H. Han, *Mater. Sci. Eng., C*, 2019, **98**, 1–8.

66 B. Muller-Bierl, H. Graf, G. Steidle and F. Schick, *Med. Phys.*, 2005, **32**, 76–84.